The Astrophysical Journal Letters, 939:L3 (8pp), 2022 November 1 https://doi.org/10.3847/2041-8213/ac959d
© 2022. The Author(s). Published by the American Astronomical Society.
OPEN ACCESS

# Metallicities of Five $z > 5$ Emission-line Galaxies in SMACS 0723 Revealed by JWST

A. J. Taylor[1], A. J. Barger[1,2,3], and L. L. Cowie[3]
[1] Department of Astronomy, University of Wisconsin–Madison, 475 N. Charter Street, Madison, WI 53706, USA; ataylor@astro.wisc.edu
[2] Department of Physics and Astronomy, University of Hawaii, 2505 Correa Road, Honolulu, HI 96822, USA
[3] Institute for Astronomy, University of Hawaii, 2680 Woodlawn Drive, Honolulu, HI 96822, USA
*Received 2022 August 12; revised 2022 September 11; accepted 2022 September 27; published 2022 October 26*

## Abstract

JWST's Early Release Observations of the lensing cluster SMACS J0723.3–7327 have given an unprecedented spectroscopic look into the high-redshift universe. These observations reveal five galaxies at $z > 5$. All five have detectable [O III]$\lambda$4363 line emission, indicating that these galaxies have high temperatures and low metallicities and that they are highly star-forming. In recent work, the metallicities of these five galaxies have been studied using various techniques. Here we summarize and compare these previous results, as well as perform our own measurements of the metallicities using improved methodologies that optimize the extraction of the emission lines. In particular, we use simultaneous line fitting and a fixed Balmer decrement correction, as well as a novel footprint measurement of the emission lines in the 2D spectra, to produce higher-fidelity line ratios that are less sensitive to calibration and systematic effects. We then compare our metallicities to those of $z \lesssim 1$ galaxies with high rest-frame equivalent widths of H$\beta$, finding that they may be good analogs. Finally, we estimate that the JWST galaxies out to $z \sim 8$ are young compared to the age of the universe.

*Unified Astronomy Thesaurus concepts:* High-redshift galaxies (734); Emission line galaxies (459); Galaxy spectroscopy (2171); Metallicity (1031)

## 1. Introduction

Prior to the launch of the James Webb Space Telescope (JWST), the rest-frame optical high-redshift universe was mostly inaccessible. While instruments such as the MOSFIRE spectrograph on the Keck II 10 m telescope can observe out to 2.4 $\mu$m, the abundance of sky lines and the diminished atmospheric transmission of 2.5–3.4 $\mu$m light have placed severe limits on our ability to observe emission-line galaxies beyond redshifts of $z \sim 3$–4. The JWST Early Release Observations (ERO) of the lensing cluster SMACS J0723.3–7327 have definitively demonstrated that these limitations no longer exist.

While previous spectroscopic studies of galaxies at $z > 5$ were primarily limited to observations of the Ly$\alpha$ line (e.g., Matthee et al. 2015; Hu et al. 2016; Santos et al. 2016; Jiang et al. 2017; Konno et al. 2018; Shibuya et al. 2018; Songaila et al. 2018, 2022; Hu et al. 2019; Taylor et al. 2020, 2021; Ning et al. 2022; Wold et al. 2022), the NIRSpec instrument on JWST now permits observations of rest-frame optical emission lines, such as [O III]$\lambda\lambda\lambda$ 5007,4959,4363 and the Hydrogen Balmer series out to $z \sim 9$. Of these lines, the [O III]$\lambda$4363 auroral line is of particular interest. This line is typically only seen in high-temperature, low-metallicity galaxies, and it serves as an excellent electron temperature ($T_e$) diagnostic when compared to the line strength of the [O III]$\lambda\lambda$ 5007,4959 complex (e.g., Pilyugin & Thuan 2005; Izotov et al. 2006; Yin et al. 2007). This "direct $T_e$ method" has been used to determine gas-phase metallicities of galaxies from the local universe to $z \sim 3$ (e.g., Kakazu et al. 2007; Brown et al. 2016; Ly et al. 2016; Indahl et al. 2021; Laseter et al. 2022). With the JWST SMACS J0723 observations, metallicities have now been measured by various authors to $z \sim 8.5$.

Original content from this work may be used under the terms of the Creative Commons Attribution 4.0 licence. Any further distribution of this work must maintain attribution to the author(s) and the title of the work, journal citation and DOI.

Carnall et al. (2022) introduced the JWST/NIRSpec sample and their spectroscopic redshifts. They used the `Pandora.ez` tool (Garilli et al. 2010) and visual inspection to determine redshifts for the 35 galaxies targeted by the microshutter array observations. They found secure redshifts for 10 galaxies, of which 5 (04590, 05144, 06355, 08140, and 10612) lie at $z > 5$. They also noted that several of the spectra showed clear detections of the [O III]$\lambda$4363 emission line.

Schaerer et al. (2022) used the level 3 1D spectra of objects 04590, 06355, and 10612 from the JWST Science Calibration Pipeline (version 1.5.3) as their data set for measuring metallicities. For each galaxy, they averaged the 1D spectra from each pointing together after masking spectral regions that were affected by cosmic rays and other artifacts. They fit Gaussian profiles to the individual emission lines in these averaged 1D spectra after assuming a flat continuum in $f_\lambda$ to measure line fluxes for [O III] $\lambda\lambda\lambda$ 5007,4959,4363, [O II]$\lambda$3727, [Ne III]$\lambda$3869, H$\beta$, H$\gamma$, and H$\delta$. They noted that the Balmer line ratios for some of the objects were nonphysical, featuring ratios larger than those predicted by Case B recombination (Osterbrock & Miller 1989). To compensate for this, they applied a power-law correction to the spectral flux fit to the Case B ratios for H$\gamma$/H$\beta$ and H$\delta$/H$\beta$. This correction loses the information on any dust attenuation. Using their corrected line fluxes, they followed Izotov et al. (2006) to derive direct $T_e$ method metallicities for their three objects. They found an unreasonably high value of $T_e$ for galaxy 04590, so they did not publish it.

Curti et al. (2022a) also calculated metallicities for objects 04590, 06355, and 10612. However, they retrieved level 2 2D spectral data products from the JWST Science Calibration Pipeline (version 1.5.3) and reprocessed them using the NIRSpec Guaranteed Time Observations (GTO) Pipeline (NIRSpec GTO collaboration 2022, in preparation) with optimized extraction apertures and bad/cosmic ray pixel masking. They also used a response function calibration based on the JWST observed calibration star 2MASS J18083474 + 6927286 (JWST Program

#1128). Through this reprocessing, they noted that one of the microshutters in the array failed to open for one of the nods in observation 7 of object 04950. They used the GTO Pipeline to combine the spectra obtained in each of the two observations, excluding the failed nod for 04950. They made their resulting 1D spectra publicly available (Curti et al. 2022b).

Curti et al. (2022a) used `PPXF` (Cappellari 2017) to fit both lines fluxes and continua measurements to the spectra. They found that their Balmer ratios also showed deviations from Case B recombination, but only in H$\delta$ and higher energy lines. They followed Nicholls et al. (2013) to determine $T_e$ and the `getIonAbundance` routine from `PYNEB` (Luridiana et al. 2012, 2015) to calculate abundances of $O^+$ and $O^{++}$ in each galaxy. They also noted a high value of $T_e$ (27,700 K) for galaxy 04590. In a separate study, Tacchella et al. (2022) used the spectra from Curti et al. (2022a) and NIRCam photometry with the `Prospector` code (Johnson et al. 2021) to infer the gas-phase metallicities of objects 04590, 06355, and 10612. Interestingly, despite masking the [O III]$\lambda$4363 line in their fits, they found broad agreement with the results of Curti et al. (2022a).

Trump et al. (2022) calculated metallicities for all five $z > 5$ galaxies starting from the level 2 2D spectral data products from the JWST Science Calibration Pipeline (version 1.5.3). They flux calibrated these spectra using simulations drawn from the NIRSpec Instrument Performance Simulator (Piquéras et al. 2010). Notably, Trump et al. (2022) found that the default 8 spatial pixel "extended" pipeline spectral extraction aperture was too large for these compact objects, instead preferring a 4 spatial pixel extraction aperture.

Trump et al. (2022) then used the IDL function `mpfit` to fit Gaussian profiles to the individual emission lines. Using the direct $T_e$ method following Nicholls et al. (2020) and Perez-Montero et al. (2021) and assuming a fixed Balmer decrement (see Section 3.2 below), they reported high values of $T_e$ for both 04590 (22,400 K) and 08140 (26,900 K). They were the first to report [O III]$\lambda$4363 detections and metallicities for objects 05144 and 08140.

Rhoads et al. (2022) released their own study of the metallicities of objects 04590, 06355, and 10612. They used the level 3 1D spectra provided by the JWST Science Calibration Pipeline (version 1.5.3). They fit Gaussian profiles to the individual emission lines for each observation (s007 and s008) separately, before averaging (with weighting) the resulting line ratios from each observation. They stated that their measured Balmer line ratios were within 1$\sigma$–2$\sigma$ of the theoretical values (Osterbrock & Miller 1989), and they did not mention any flux recalibrations. They used the direct $T_e$ method detailed in Jiang et al. (2019), which was based on Izotov et al. (2006). They reported a very high $T_e$ (37,000 K) for galaxy 04590, even exceeding those reported by Curti et al. (2022a) and Trump et al. (2022).

Given the broad range of methodologies, software, calibrations, and corrections used in the literature to study these five galaxies, our goals in this work are to summarize these methods and results (see Tables 1 and 2) and to perform our own measurements using improved methodologies that are less sensitive to calibration and flux extraction systematics. Additionally, we will compare our metallicities with those of a sample of extreme emission-line galaxies at $z \lesssim 1$ from Laseter et al. (2022) as a function of the measured rest-frame equivalent width (EW) of the H$\beta$ line.

## 2. Observations

We analyze the JWST ERO of SMACS J0723 from Program #2736, focusing on the NIRSpec observations of objects 04590, 05144, 06355, 08140, and 10612—the five galaxies with spectroscopic redshifts $z > 5$ from Carnall et al. (2022). These observations were taken using the NIRSpec microshutter array in two pointings (s007 and s008) using both the G235M/F170LP and G395M/F290LP grating/filter combinations. Each combination of pointings and gratings/filters were observed for 8754 s. Specifically, we analyze the G395M/F290LP observations for objects 04950, 05144, 06355, and 10612, and the G235M/F170LP observations for object 08140. We use the level 3 1D and 2D spectral data products from the JWST Science Calibration Pipeline (version 1.5.3).

## 3. Analysis

### 3.1. Emission-line Measurement and Spectral Calibration

In our initial examination of the 1D (`x1d`) spectra, we found the same microshutter (for object 04590) and contamination problems previously noted in the literature. To minimize these and avoid any unwanted effects resulting from differences in total flux calibration between the two observations for each object, we masked areas affected by large, nonphysical spikes in the spectral flux greater than the peak of the [O III]$\lambda$5007 line before coadding the two spectra. We propagated the masked regions of each spectrum to the combined spectrum, preferring to exclude the union of these masked regions rather than introduce problems from unmatched flux calibrations between the two observations. Before measuring line fluxes, we converted the summed spectra from units of $f_\nu$ to units of $f_\lambda$.

We measured emission-line fluxes in three groups: [O III]$\lambda\lambda$ 5007,4959 + H$\beta$, [O III]$\lambda$4363 + H$\gamma$, and [O II]$\lambda$3727+H8+ [Ne III]$\lambda$3869. For each group of lines, we simultaneously fit Gaussian functions and a linear continuum (in $f_\lambda$) to the spectrum using the `scipy` function `curve_fit` (Virtanen et al. 2020). When fitting [O III]$\lambda\lambda$ 5007,4959 + H$\beta$, we enforced a common line width for all three lines, as well as fixed ratios of the line centers and a fixed 3:1 ratio of the [O III] $\lambda$5007 to [O III]$\lambda$4959 line ratios. Similarly, when fitting [O III] $\lambda$4363 + H$\gamma$ and [O II]$\lambda$3727+H8+[Ne III]$\lambda$3869, we required a common line width for the lines and a fixed ratio of the line centers for each group. This procedure is helpful for compensating for regions of the [O III]$\lambda\lambda$ 5007,4959 doublet that are masked due to contamination (for example, in 04590), as well as for better fitting relatively faint lines, such as [O III] $\lambda$4363, by allowing the more strongly detected H$\gamma$ line to influence the line center and line width fits. Fitting faint lines with single Gaussians generally results in upward biasing. We show the results of these emission-line fits in Figure 1.

Visually, it is clear that objects 04590, 06355, and 10612 are reasonably well fit by the Gaussian functions and fitting constraints, while the lack of any meaningful [O III]$\lambda$4363 detection and overall lower signal-to-noise ratio (S/N) in objects 05144 and 08140 result in unusable fits. This is consistent with 05144 and 08140 only being analyzed after the data reprocessing in Trump et al. (2022) and being excluded from the other recent works.

Due to these nondetections and the overall high noise levels in 05144 and 08140, we now turn to the 2D spectra (`s2d`). While Curti et al. (2022a) and Trump et al. (2022) elected to recalibrate the level 2 2D spectra, our methods do not require a

**Table 1**
Methods

| Study | Initial Data | Calibration | Line Measurement | Balmer Correction | Metallicity Prescription |
|---|---|---|---|---|---|
| This work: 1D | Level 3 1D Spectra | JWST Pipeline | Simultaneous Gaussian line and linear continuum fits | Fixed $H\gamma/H\beta = 0.47$ | Izotov et al. (2006) |
| This work: 2D | Level 3 2D Spectra | JWST Pipeline | Weighted extraction simultaneous Gaussian line and linear continuum fits | Fixed $H\gamma/H\beta = 0.47$ | Izotov et al. (2006) |
| This work: footprint | Level 3 2D Spectra | JWST Pipeline | 2D footprints | Fixed $H\gamma/H\beta = 0.47$ | Izotov et al. (2006) |
| Schaerer et al. (2022) | Level 3 1D Spectra | JWST Pipeline | Gaussian line and flat continuum fits | Power-law fit | Izotov et al. (2006) |
| Curti et al. (2022a) | Level 2 2D count-rate maps | GTO Pipeline | `PPXF` fitting | None | Nicholls et al. (2013), `PYNEB` |
| Trump et al. (2022) | Level 2 2D count-rate maps | NIRSpec Simulator | 4 pixel 2D extraction Gaussian line fits | Fixed $H\gamma/H\beta = 0.47$ | Nicholls et al. (2020), Perez-Montero et al. (2021) |
| Rhoads et al. (2022) | Level 3 1D Spectra | JWST Pipeline | Simultaneous Gaussian line and local continuum fits | None | Jiang et al. (2019), Izotov et al. (2006) |

**Table 2**
Metallicities and Electron Temperatures

| Object<br>Redshift ($z$) | 04590<br>8.4989 | 05144<br>6.3805 | 06355<br>7.6687 | 08140<br>5.2753 | 10612<br>7.6607 |
|---|---|---|---|---|---|
| 1D 12+log(O/H) | $6.84^{+0.08}_{-0.07}$ | … | $7.89^{+0.07}_{-0.07}$ | … | $7.82^{+0.15}_{-0.11}$ |
| 2D 12+log(O/H) | $6.98^{+0.97}_{-0.15}$ | $7.69^{+0.28}_{-0.17}$ | $8.06^{+0.20}_{-0.11}$ | … | $7.72^{+0.31}_{-0.10}$ |
| Footprint 12+log(O/H) | $6.82^{+0.29}_{-0.10}$ | $7.63^{+0.22}_{-0.23}$ | $8.03^{+0.19}_{-0.17}$ | $7.68^{+0.51}_{-0.50}$ | $7.67^{+0.21}_{-0.21}$ |
| Schaerer et al. (2022) 12+log(O/H) | … | … | 7.85 | … | 7.85 |
| Curti et al. (2022a) 12+log(O/H) | $6.99 \pm 0.11$ | … | $8.24 \pm 0.07$ | … | $7.73 \pm 0.12$ |
| Trump et al. (2022) 12+log(O/H) | <7.75 | 7.98 | 8.18 | <7.75 | 7.95 |
| Rhoads et al. (2022) 12+log(O/H) | $6.88 \pm 0.15$ | … | $8.09 \pm 0.16$ | … | $7.68 \pm 0.24$ |
| 1D $T_e$ ($10^4$ K) | $3.38^{+0.35}_{-0.34}$ | … | $1.49^{+0.09}_{-0.09}$ | … | $1.72^{+0.20}_{-0.20}$ |
| 2D $T_e$ ($10^4$ K) | $2.87^{+0.82}_{-1.15}$ | $1.79^{+0.27}_{-0.31}$ | $1.37^{+0.12}_{-0.16}$ | … | $1.79^{+0.17}_{-0.33}$ |
| Footprint $T_e$ ($10^4$ K) | $3.48^{+0.42}_{-0.96}$ | $1.83^{+0.37}_{-0.25}$ | $1.44^{+0.17}_{-0.16}$ | $1.77^{+0.14}_{-1.77}$ | $1.83^{+0.34}_{-0.25}$ |
| Schaerer et al. (2022) $T_e$ ($10^4$ K) | … | … | 1.60 | … | 1.87 |
| Curti et al. (2022a) $T_e$ ($10^4$ K) | $2.77 \pm 0.42$ | … | $1.20 \pm 0.07$ | … | $1.75 \pm 0.16$ |
| Trump et al. (2022) $T_e$ ($10^4$ K) | 2.24 | 1.58 | 1.29 | 2.69 | 1.58 |
| Rhoads et al. (2022) $T_e$ ($10^4$ K) | $3.72 \pm 0.99$ | … | $1.34 \pm 0.16$ | … | $2.19 \pm 0.54$ |

**Note.** We convert the $Z/Z_\odot$ values for metallicity given in Trump et al. (2022) to 12+log(O/H) assuming a solar abundance of 8.75 (Bergemann et al. 2021).

robust absolute flux calibration. Rather, we require only a firm relative flux calibration over short (<150 Å rest-frame) spans in wavelength. As a result, the lack of flux calibrations in the level 3 2D spectra are inconsequential to our study. To prepare these data for emission-line measurements, we first coadded the two observations for each object. As with the 1D spectra, before measuring line fluxes, we converted from units of $f_\nu$ to units of $f_\lambda$. From these coadded 2D spectra, we performed emission-line fitting and extraction using two different methods.

First, we used a weighted spectral extraction to extract 1D spectra from the now coadded 2D spectra. While the level 3 1D spectra and Trump et al. (2022) used fixed extraction apertures (of 8 pixels and 4 pixels, respectively), we instead used a weighting scheme. For each object, we examined the region around the [O III]$\lambda$5007 line—the highest signal emission feature—in a 20 Å window. We summed the flux in this region over the spectral direction to construct a 1D spatial line profile. We renormalized this line profile so that its peak value was 1, making it usable as a spatial weighting function. We then applied this weighting function to the 2D spectrum and summed over the spatial axis to produce a 1D spectrum. Finally, we fit the emission lines using the same methodology that we used on the original 1D spectra.

We show our extracted 1D spectra and the corresponding emission-line fits in Figure 2. In all cases, the noise in the spectral continuum relative to the emission-line strengths is greatly decreased for all five objects relative to the original 1D spectra. Objects 05144 and 10612 show more consistent [O III] $\lambda\lambda$ 5007,4959 internal line ratios, and the contamination around the H$\beta$ line in 10612 is completely eliminated. Most notably, the new spectrum for object 05144 shows clear and well-fit [O III]$\lambda$4363 emission where the original 1D spectrum showed only noise. Only object 08140 fails to show any

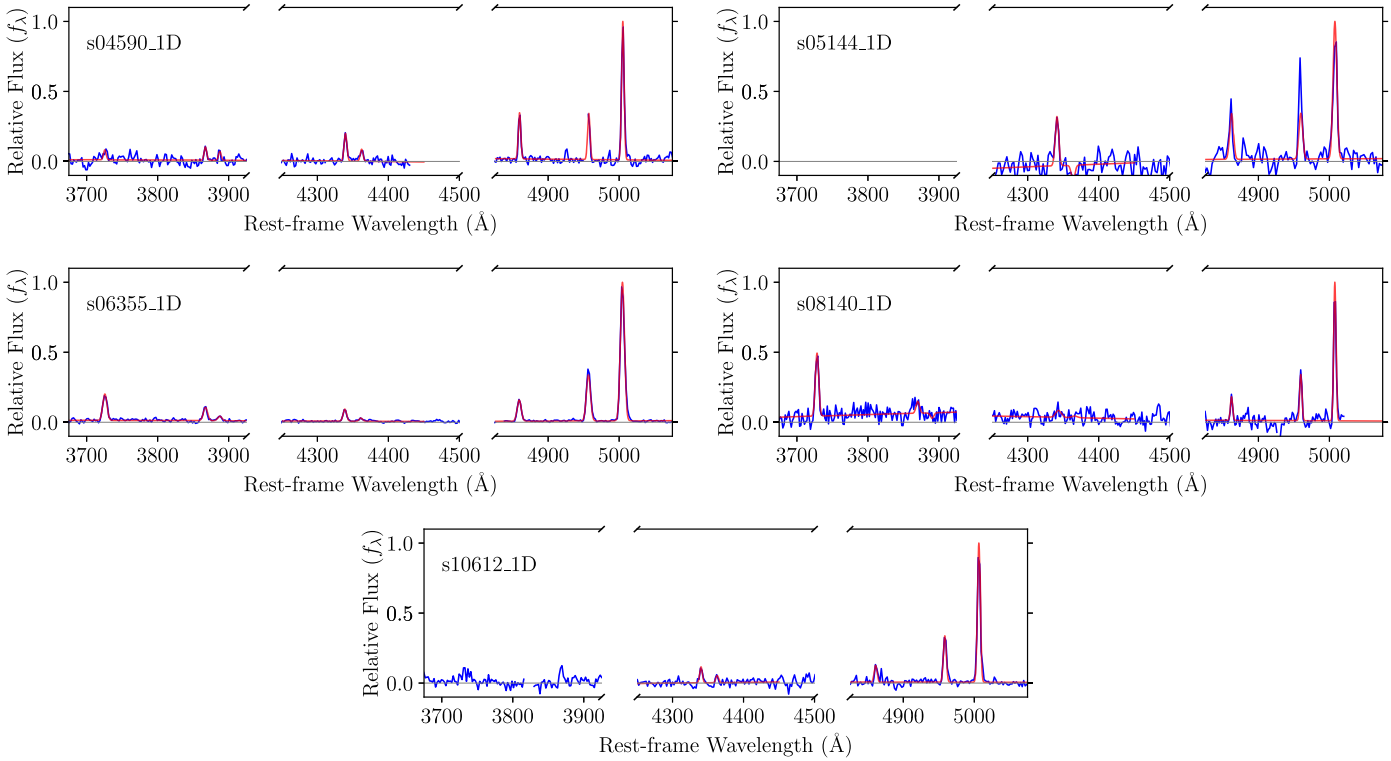


**Figure 1.** Gaussian and continuum fits to the 1D spectra for the galaxy sample. In each panel, the blue curve is the coadded 1D spectrum, and the red curves are the best-fit functions to the spectrum. For visual clarity, we normalize the flux scale to be equal to 1 at the peak of the [O III]$\lambda$5007 line fit. Note that object 05144 is at too low of redshift for the G395/F290LP observations to capture the [O II]$\lambda$3727+H8+[Ne III]$\lambda$3869 complex. To avoid introducing errors from comparing lines across both filter/grating observations, we omit the [O II]$\lambda$3727+H8+[Ne III]$\lambda$3869 fit for this object. Also note that due to limited signal, the [O II]$\lambda$3727+H8+[Ne III] $\lambda$3869 fit for object 10612 failed to converge.

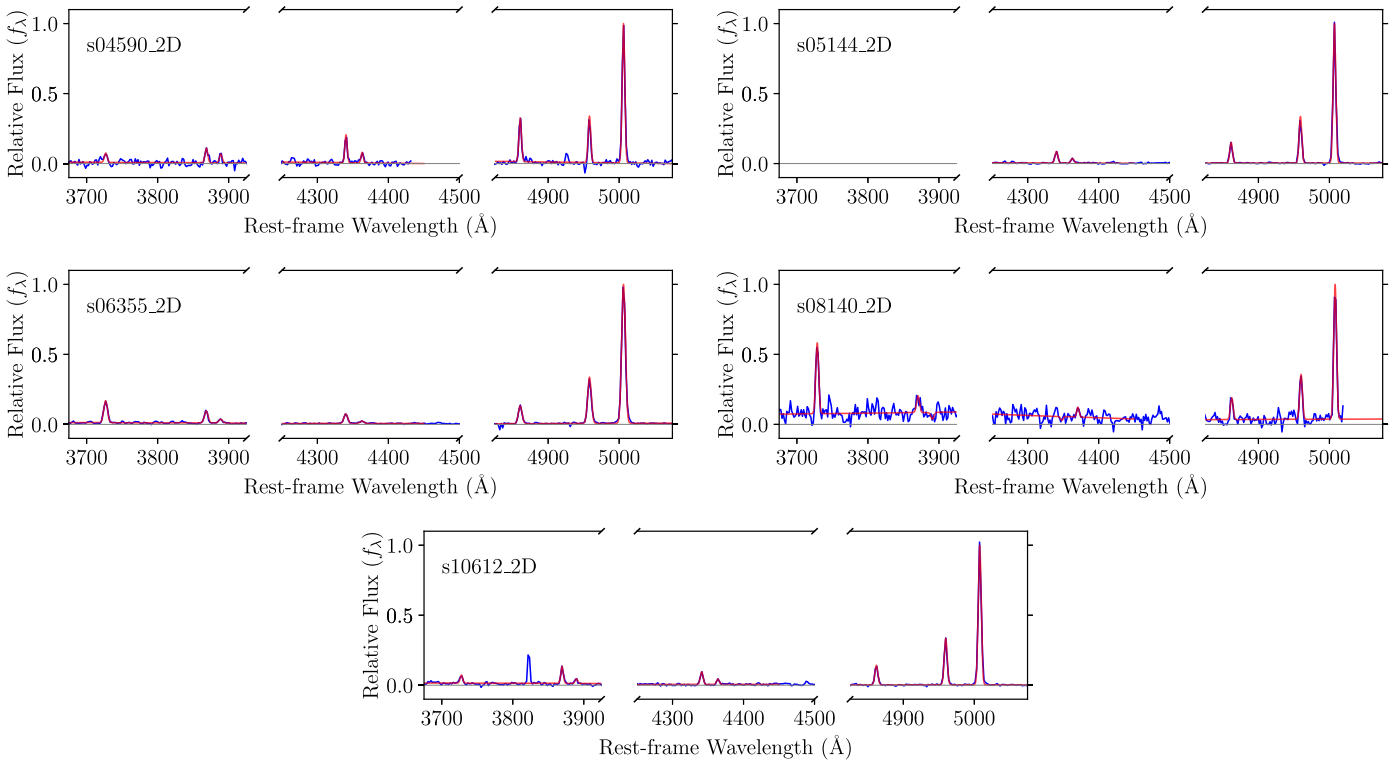


**Figure 2.** Gaussian and continuum fits to the weighted aperture extracted 1D spectra for the galaxy sample. In each panel, the blue curve is the coadded and extracted 1D spectrum, and the red curves are the best-fit functions to the spectrum. For visual clarity and ease of comparison, we again normalize the flux scale to be equal to 1 at the peak of the [O III]$\lambda$5007 line fit.

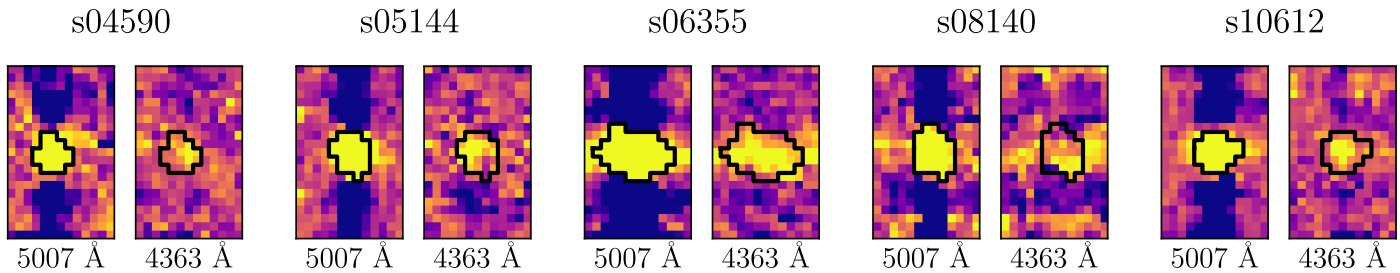


**Figure 3.** Cutouts of the coadded 2D spectra centered on the [O III]$\lambda$5007 and [O III]$\lambda$4363 lines. The extraction footprints determined by the [O III]$\lambda$5007 line shape are shown with black outlines.

significant H$\gamma$ or [O III]$\lambda$4363 emission above the continuum noise level. This weighted extraction removes any systematics introduced in the choice of a fixed extraction aperture. The weighted scheme best captures the line and continuum flux of an object based on its individual spatial point-spread characteristics for extraction into a 1D spectrum.

In an attempt to further increase the signal in object 08140, we implemented one final flux measurement technique. Here we again used our coadded 2D spectra. However, instead of using weighted spatial apertures to produce a 1D spectrum for line flux measurements, we performed direct line flux extraction in the 2D spectra.

We first analyzed the [O III]$\lambda$5007 line and fit its 2D footprint in the 2D spectrum by eye. We summed the flux in this footprint to measure the [O III]$\lambda$5007 line flux. We then translated this footprint to the positions of the other emission lines of interest. At each position, we again summed the flux within the footprint to measure that line's flux. To remove the underlying continuum at each line measurement, we used the same footprint to sample the continuum at random positions near the emission lines of interest, and we subtracted the median of these measurements from each line flux. We show these [O III]$\lambda$5007 extraction footprints in Figure 3.

Using this method, we detected faint but measurable [O III] $\lambda$4363 flux in object 08140, sufficient for calculating its metallicity. We consider this flux measurement method to be superior to 1D spectral fitting and 2D spectral weighted extraction, as it inherently removes any systematic effects introduced by noise or contamination along the spatial axis. Directly measuring the line fluxes in the 2D spectra based on the shape of the highest S/N line better captures the emission signal of both strong and faint lines by better excluding nearby nonemission pixels that would otherwise introduce additional noise or continuum contributions to the measurements.

To estimate the uncertainties on these line flux measurements, we performed Monte Carlo simulations for each object and methodology. For a given 1D or 2D spectrum, we constructed an array of Gaussian distributions centered at the flux values of the spectra with standard deviations given by the flux errors provided in the 1D and 2D data files. We sampled these distributions 5000 times for each object and method and reextracted the line fluxes from the resulting spectra. We then took the 16th and 84th percentile of each of the resulting distributions as the 1$\sigma$ confidence interval for the line flux and EW measurements.

We compare the performance and fidelity of all of these techniques in Section 4.

### 3.2. Metallicity Calculations

To calculate the metallicities for all our methodologies, we followed Laseter et al. (2022), who used the direct $T_e$ method described in Izotov et al. (2006, which was also used by Schaerer et al. 2022 and Rhoads et al. 2022). This means we will be able to make direct comparisons with Laseter et al.'s (2022) $z \lesssim 1$ extreme emission-line galaxy sample in Section 4.1.

In this method, the line ratios of [O III]$\lambda\lambda$ 5007,4959 and [O III] $\lambda$4363 are used to derive an [O III] $T_e$. This $T_e$ may then be used with the [O III]$\lambda\lambda$ 5007,4959 to H$\beta$ and [O II]$\lambda$3727 to H$\beta$ line ratios to derive the abundances of $O^+$/H and $O^{++}$/H (see Equations (1), (2), (3), and (5) in Izotov et al. 2006).

Again following Laseter et al. (2022), we adopted a modification to this method (also used by Trump et al. 2022), where instead of measuring the ratio of [O III]$\lambda\lambda$ 5007,4959 to [O III]$\lambda$4363 directly, we instead used the following equation:

$$\frac{[\mathrm{O\,III}]_{5007,4959}}{[\mathrm{O\,III}]_{4363}} = \frac{[\mathrm{O\,III}]_{5007,4959}}{\mathrm{H}\beta} \times \frac{\mathrm{H}\gamma}{[\mathrm{O\,III}]_{4363}} \times 0.47. \quad (1)$$

This equation relates the [O III] lines to nearby hydrogen lines and enforces a H$\gamma$/H$\beta$ Balmer decrement equal to the extinction-free Case B recombination value of 0.47 (Osterbrock & Miller 1989). This helps to correct for any relative miscalibration of the observed spectral flux as a function of wavelength by considering ratios of nearby (<150 Å rest-frame) lines before using the Balmer decrement to compare these flux ratios across the much larger ~640 Å (rest-frame) span. It also implicitly corrects the line ratios for any dust extinction.

Similarly, to ensure a proper ratio of [O II]$\lambda$3727 to H$\beta$, we use the H8/H$\beta$ Case B recombination value of 0.107 (Osterbrock & Miller 1989):

$$\frac{[\mathrm{O\,II}]_{3727}}{\mathrm{H}\beta} = \frac{[\mathrm{O\,II}]_{3727}}{\mathrm{H8}} \times 0.107. \quad (2)$$

To estimate the uncertainties on our measurements of $T_e$ and metallicity, we extend the Monte Carlo simulations described in Section 3.1 to recalculate the $T_e$ and metallicity for each Monte Carlo run. We again take the 16th and 84th percentile of each of the resulting distributions of $T_e$ and metallicity as the 1$\sigma$ confidence interval for the measurements.

## 4. Results

The metallicity results from this work and from the literature demonstrate reasonable agreement across all five objects (see Table 2). Our 1D spectral results most closely resemble the results of Schaerer et al. (2022), who also used the level 3 1D spectra. Interestingly, Rhoads et al. (2022) used the same 1D spectra, but their results show values more similar to our 2D methods.

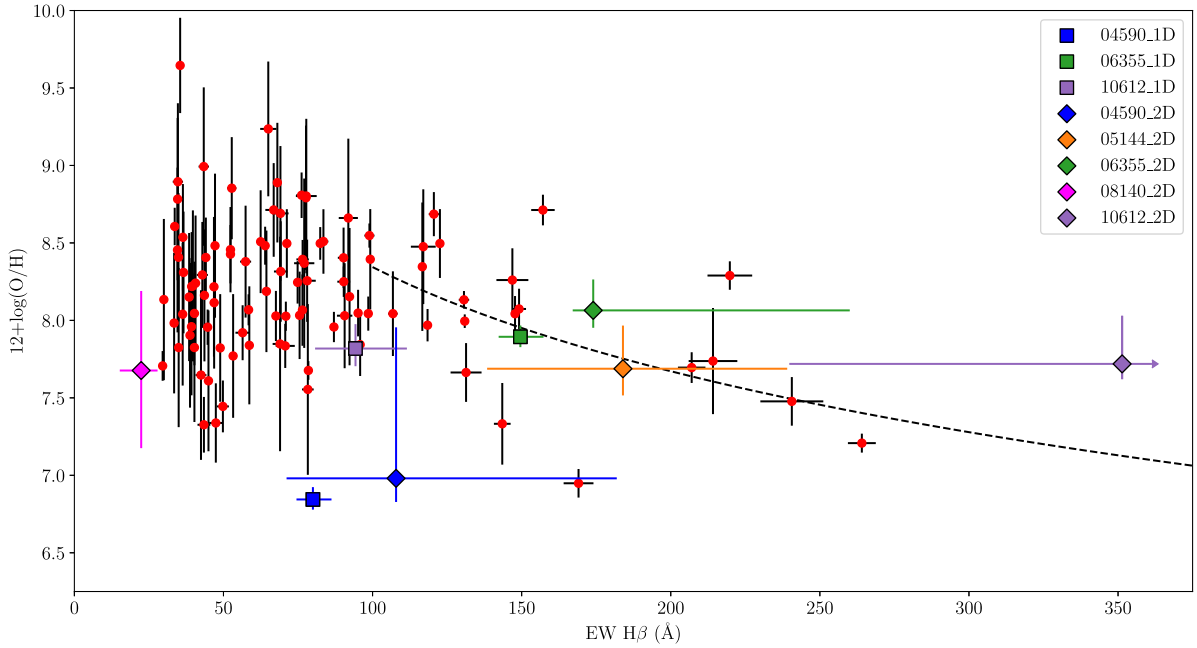


**Figure 4.** Metallicity vs. rest-frame EW(H$\beta$) for the Laseter et al. (2022) sample of galaxies at $z \lesssim 1$ with strong emission lines and rest-frame EW(H$\beta$) > 30 Å (red circles), JWST 1D spectra results (squares, see legend for colors), and JWST 2D spectra results (diamonds, see legend for colors). Note that the 2D spectrum for object 05144 has very faint continuum near the H$\beta$ line. Given the substantial error on the continuum for this object, the upper error bounds on the EW(H$\beta$) exceed ~400 Å, so we use a rightward-pointing arrow. Note that as object 08140 only showed an [O III]$\lambda$4363 detection with the footprint method, we use that metallicity with the 2D EW(H$\beta$) (pink diamond). The black dashed curve is the best fit to 12+log(O/H) vs. EW(H$\beta$) for values of EW(H$\beta$) > 100 Å from Laseter et al. (2022).

Our 2D and footprint methods show strong agreement with one another and most closely resemble the results of Rhoads et al. (2022). The results of Trump et al. (2022) seem to be consistently ~0.2 dex higher than our own. Interestingly, Trump et al. (2022) reported using a Balmer decrement correction identical to our own (see their Equation (1) and our Equation (1)), so we attribute the differences in calculated metallicity to their use of the Perez-Montero et al. (2021) metallicity estimator instead of that of Izotov et al. (2006); the former has a flatter slope in metallicity as a function of $T_e$ at $T_e > 15{,}000$ K.

The results from Curti et al. (2022a) are also ~0.1 dex higher than our 2D methods, but they show general agreement within the error bounds of both studies. Especially given its performance in detecting [O III]$\lambda$4363 in object 08140, we believe that our footprint extraction method is the best method for line flux measurements, as it helps to avoid any aperture effects, as well as noise along the spatial axis and any effects from the "nods" in the 2D data.

For all of the objects, we find that the contributions to the overall 12+log(O/H) abundance from $O^+$ are $\lesssim$10% of the contribution from $O^{++}$, indicating that these objects are all highly ionized.

For $T_e$, all of the studies seem to agree with one other within their error bounds. We note—echoing the remarks from the literature—that all values of $T_e$ calculated for object 04590 are unphysically high, or at the upper bound of reasonability. Of all the studies, the recalibrated spectra from Curti et al. (2022a) and Trump et al. (2022) give the lowest values. The large uncertainty in our 2D results for the $T_e$ for object 04590 (and the corresponding large uncertainty in metallicity) also reflect the relatively poor data quality in the 04590 spectra. Due to these uncertain measurements of $T_e$ (the result of extraordinarily bright [O III]$\lambda$4363 emission relative to [O III]$\lambda\lambda$ 5007,4959), the galaxy's high redshift of $z = 8.4989$ (Schaerer et al. 2022), and the partial data contamination from a malfunctioning microshutter, 04590 may warrant additional JWST or other multiwavelength follow-up.

### 4.1. Metallicity and Hβ Equivalent Width

Laseter et al. (2022) presented a correlation between direct $T_e$ metallicity and rest-frame EW(H$\beta$) at rest-frame EW(H$\beta$) > 100 Å (Spearman rank coefficient = − 0.469, $p = 0.037$) using a sample of emission-line galaxies at $z \lesssim 1$ observed with the DEIMOS multiobject spectrograph on the Keck II 10 m telescope. They proposed that galaxies with high rest-frame EW(H$\beta$) may serve as analogs to some of the earliest galaxies. Given the high redshifts of the present sample, we now make comparisons with the Laseter et al. (2022) sample.

We measured the EWs for the 1D and 2D weighted aperture extracted spectra through the simultaneous fitting of the H$\beta$ (and [O III]$\lambda\lambda$ 5007,4959) line fluxes and the nearby continuum flux density level. Since we shifted the wavelength scale to the rest frame in the first step of our fitting, dividing the integrated line flux by the continuum flux density provides the proper rest-frame line EW.

Objects 04590, 06355, and 08140 show the strongest continuum detections in both their 1D and 2D spectra, which is reflected in their lower EWs and in their relatively smaller error bounds (see Figure 4). For object 10612, the 2D spectrum shows very weak continuum emission. As a result, 10612 exhibits a very high (>300 Å) 2D EW(H$\beta$) with very large error bounds due to the high fractional flux error in the continuum measurement. Due to the fixed size 2D to 1D flux extraction apertures from the JWST Pipeline and the lack of 1D [O III]$\lambda$4363 detections for objects 05144 and 08140, we consider the 2D EWs—despite their large error bounds—to be the better (if less certain) measurements of EW(H$\beta$) for

all five objects. Moreover, we agree with the claims of Trump et al. (2022), Rhoads et al. (2022), and Brinchmann (2022) that the uncertainties provided for the 1D spectra underestimate the true uncertainties by a factor of ∼2. Thus, our calculated uncertainties for the 1D EW(H$\beta$) are likely also underestimated.

We compare our results with the Laseter et al. (2022) sample in Figure 4, finding good agreement. The objects with 2D EW(H$\beta$) > 100 Å (04590, 05144, 06355, and 10612) deviate from the Laseter et al. (2022) best-fit 12+log(O/H) curve by −1.29, −0.06, 0.26, and 0.59 dex, respectively. Given the before-mentioned high $T_e$ for object 04950 and the large uncertainty in EW(H$\beta$) for object 10612, the sample shows reasonable agreement with the Laseter et al. (2022) curve. This suggests that low-redshift, high-EW(H$\beta$) objects may indeed be good analogs of early galaxies at $z \sim 5$–9.

Laseter et al. (2022) also fit a metallicity–EW(H$\beta$)–age relation in their study for galaxies with EW(H$\beta$ > 100 Å), assuming a continuous starburst model. Using their relation of $\log t_{\rm years} = 12 + \log {\rm O/H} - 0.93$ and our best footprint method metallicities, we estimate galaxy ages of 04590: $0.8^{+0.7}_{-0.2}$, 05144: $5.1^{+3.5}_{-2.1}$, 06355: $12.6^{+6.9}_{-4.1}$, 08140: $5.6^{+12.6}_{-3.4}$, and 10612: $5.5^{+3.5}_{-2.1}$ Myr. Even 12.6 Myr for object 06355—the oldest estimated galaxy age in the sample—is reasonable, as the age of the universe was ∼660 Myr at $z = 7.6687$ (assuming a flat cosmology with $\Omega_{\rm M} = 0.3$, $\Omega_\Lambda = 0.7$, and $H_0 = 70\ {\rm km\ s^{-1}\ Mpc^{-1}}$).

Carnall et al. (2022) used `Bagpipes` (Carnall et al. 2018) to estimate mean stellar ages of 04950: $2^{+10}_{-1}$, 05144: $1.2^{+0.3}_{-0.2}$, 06355: $1.2^{+0.3}_{-0.2}$, 08140: $19^{+21}_{-10}$, and 10612: $1.2^{+0.3}_{-0.2}$ Myr. Using `Prospector` fitting, Tacchella et al. (2022) found half-mass times ($t_{50}$) of 04950: $5^{+102}_{-3}$, 06355: $3^{+29}_{-1}$, and 10612: $7^{+96}_{-4}$ Myr. While these different age metrics are not directly comparable with one another, our estimates show reasonable agreement with both Carnall et al. (2022) and Tacchella et al. (2022) within the stated uncertainties and differences in spectral calibration.

## 5. Summary

In this work, we measured gas-phase metallicities for the five $z > 5$ emission-line galaxies from the JWST ERO of SMACS 0723. We measured lines fluxes from these data using improved 1D and 2D spectral methods, which we consider to be optimal. We then computed metallicities using the direct $T_e$ method. We compared our results with those in the literature and found reasonably good agreement within the provided error bounds, which is encouraging given the variety of data processing and line ratio measurement methodologies utilized.

We found that the metallicities and EW(H$\beta$) of the $z > 5$ galaxies roughly follow the trends of Laseter et al.'s (2022) sample of $z \lesssim 1$ high rest-frame EW(H$\beta$) galaxies, offering support that they may be low-redshift analogs to the early galaxies seen with JWST. Finally, we estimated that the high-redshift galaxies are young compared to the age of the universe.

We thank the anonymous reviewer and data editor for their constructive report that helped us to improve this work.

We gratefully acknowledge the William F. Vilas Estate (A.J. T.) and a Kellett Mid-Career Award and a WARF Named Professorship from the University of Wisconsin-Madison Office of the Vice Chancellor for Research and Graduate Education with funding from the Wisconsin Alumni Research Foundation (A.J.B.).

This work is based on observations made with the NASA/ESA/CSA James Webb Space Telescope (JWST). The data were obtained from the Mikulski Archive for Space Telescopes (MAST) at the Space Telescope Science Institute, which is operated by the Association of Universities for Research in Astronomy, Inc., under NASA contract NAS 5–03127 for JWST. These observations are associated with program #2736. The specific observations analyzed can be obtained from MAST via doi:10.17909/espg-fy96.

The Early Release Observations and associated materials were developed, executed, and compiled by the ERO production team: Hannah Braun, Claire Blome, Matthew Brown, Margaret Carruthers, Dan Coe, Joseph DePasquale, Nestor Espinoza, Macarena Garcia Marin, Karl Gordon, Alaina Henry, Leah Hustak, Andi James, Ann Jenkins, Anton Koekemoer, Stephanie LaMassa, David Law, Alexandra Lockwood, Amaya Moro-Martin, Susan Mullally, Alyssa Pagan, Dani Player, Klaus Pontoppidan, Charles Proffitt, Christine Pulliam, Leah Ramsay, Swara Ravindranath, Neill Reid, Massimo Robberto, Elena Sabbi, and Leonardo Ubeda. The EROs were also made possible by the foundational efforts and support from the JWST instruments, STScI planning and scheduling, and Data Management teams.

*Facility:* JWST.

*Software:* astropy (Astropy Collaboration et al. 2013, 2018).

## ORCID iDs

A. J. Taylor https://orcid.org/0000-0003-1282-7454
A. J. Barger https://orcid.org/0000-0002-3306-1606
L. L. Cowie https://orcid.org/0000-0002-6319-1575

## References

Astropy Collaboration, Price-Whelan, A. M., SipHocz, B. M., et al. 2018, AJ, 156, 123
Astropy Collaboration, Robitaille, T. P., Tollerud, E. J., et al. 2013, A&A, 558, A33
Bergemann, M., Hoppe, R., Semenova, E., et al. 2021, MNRAS, 508, 2236
Brinchmann, J. 2022, MNRAS, submitted (arXiv:2208.07467)
Brown, J. S., Martini, P., & Andrews, B. H. 2016, MNRAS, 458, 1529
Cappellari, M. 2017, MNRAS, 466, 798
Carnall, A. C., McLeod, D. J., McLure, R. J., et al. 2022, MNRAS, submitted (arXiv:2208.00986)
Carnall, A. C., McLure, R. J., Dunlop, J. S., & Dave, R. 2018, MNRAS, 480, 4379
Curti, M., D'Eugenio, F., Carniani, S., et al. 2022a, MNRAS, in press
Curti, M., D'Eugenio, F., Carniani, S., et al. 2022b, The Chemical Enrichment in the early Universe as Probed by JWST via Direct Metallicity Measurements at z~8, v1, Zenodo, doi:10.5281/zenodo.6940561
Garilli, B., Fumana, M., Franzetti, P., et al. 2010, PASP, 122, 827
Hu, E. M., Cowie, L. L., Songaila, A., et al. 2016, ApJL, 825, L7
Hu, W., Wang, J., Zheng, Z.-Y., et al. 2019, ApJ, 886, 90
Indahl, B., Zeimann, G., Hill, G. J., et al. 2021, ApJ, 916, 11
Izotov, Y. I., Stasińska, G., Meynet, G., Guseva, N. G., & Thuan, T. X. 2006, A&A, 448, 955
Jiang, L., Shen, Y., Bian, F., et al. 2017, ApJ, 846, 134
Jiang, T., Malhotra, S., Rhoads, J. E., & Yang, H. 2019, ApJ, 872, 145
Johnson, B. D., Leja, J., Conroy, C., & Speagle, J. S. 2021, ApJS, 254, 22
Kakazu, Y., Cowie, L. L., & Hu, E. M. 2007, ApJ, 668, 853
Konno, A., Ouchi, M., Shibuya, T., et al. 2018, PASJ, 70, S16
Laseter, I. H., Barger, A. J., Cowie, L. L., & Taylor, A. J. 2022, ApJ, 935, 150
Luridiana, V., Morisset, C., & Shaw, R. A. 2012, in IAU Symp. 283, Planetary Nebulae: An Eye to the Future, ed. A. Manchado, L. Stanghelli, & D. Schönberner (Cambridge: Cambridge Univ. Press), 422
Luridiana, V., Morisset, C., & Shaw, R. A. 2015, A&A, 573, A42
Ly, C., Malkan, M. A., Rigby, J. R., & Nagao, T. 2016, ApJ, 828, 67

Matthee, J., Sobral, D., Santos, S., et al. 2015, MNRAS, 451, 400
Nicholls, D. C., Dopita, M. A., Sutherland, R. S., Kewley, L. J., & Palay, E. 2013, ApJS, 207, 21
Nicholls, D. C., Kewley, L. J., & Sutherland, R. S. 2020, PASP, 132, 033001
Ning, Y., Jiang, L., Zheng, Z.-Y., & Wu, J. 2022, ApJ, 926, 230
Osterbrock, D. E., & Miller, J. S. 1989, Astrophysics of Gaseous Nebulae and Active Galactic Nuclei (Mill Valley, CA: Univ. Science Books)
Pérez-Montero, E., Amorin, R., Sánchez Almeida, J., et al. 2021, MNRAS, 504, 1237
Pilyugin, L. S., & Thuan, T. X. 2005, ApJ, 631, 231
Piquéras, L., Legros, E., Pons, A., et al. 2010, Proc. SPIE, 7738, 773812
Rhoads, J. E., Wold, I. G. B., Harish, S., et al. 2022, ApJL, submitted (arXiv:2207.13020)
Santos, S., Sobral, D., & Matthee, J. 2016, MNRAS, 463, 1678
Schaerer, D., Marques-Chaves, R., Oesch, P., et al. 2022, A&A, 665, L4
Shibuya, T., Ouchi, M., Harikane, Y., et al. 2018, PASJ, 70, S15
Songaila, A., Barger, A. J., Cowie, L. L., Hu, E. M., & Taylor, A. J. 2022, ApJ, 935, 52
Songaila, A., Hu, E. M., Barger, A. J., et al. 2018, ApJ, 859, 91
Tacchella, S., Johnson, B. D., Robertson, B. E., et al. 2022, MNRAS, submitted (arXiv:2208.03281)
Taylor, A. J., Barger, A. J., Cowie, L. L., Hu, E. M., & Songaila, A. 2020, ApJ, 895, 132
Taylor, A. J., Cowie, L. L., Barger, A. J., Hu, E. M., & Songaila, A. 2021, ApJ, 914, 79
Trump, J. R., Haro, P. A., Simons, R. C., et al. 2022, ApJ, submitted (arXiv:2207.12388)
Virtanen, P., Gommers, R., Oliphant, T. E., et al. 2020, NatMe, 17, 261
Wold, I. G. B., Malhotra, S., Rhoads, J., et al. 2022, ApJ, 927, 36
Yin, S. Y., Liang, Y. C., Hammer, F., et al. 2007, A&A, 462, 535